Electronic Supplementary Material (ESI) for Nanoscale.
This journal is © The Royal Society of Chemistry 2022

Supplementary Information for

A phase field model combined with genetic algorithm for polycrystalline hafnium zirconium oxide ferroelectrics

Sandeep Sugathan [a], *Krishnamohan Thekkepat* [b,c], *Soumya Bandyopadhyay* [a], *Jiyoung Kim* [d] *and Pil-Ryung Cha* [a,*]

[a]School of Advanced Materials Engineering, Kookmin University, Seoul 02707, Korea.

[b]Electronic Materials Research Center, Korea Institute of Science and Technology, Seoul 02792, Republic of Korea.

[c]Division of Nano & Information Technology, KIST School, Korea University of Science and Technology, Seoul 02792, Republic of Korea.

[d]Department of Materials Science and Engineering, The University of Texas at Dallas, 800 West Campbell Road, Richardson, Texas 75080, USA.

*Email: cprdream@kookmin.ac.kr

KEYWORDS: HZO, phase field model, genetic algorithm, Landau coefficients, ferroelectrics

S1 Phase field microelasticity method

We describe the heterogeneous solid, i.e., polycrystalline thin film on a substrate, together with the surrounding vacuum by introducing an order parameter ζ ($\zeta = 0$ in the vacuum and $\zeta = 1$ in the thin film) following a similar approach reported in the literature[1–3]. The position dependent elastic modulus $C_{ijkl}(\mathbf{r})$ also changes the value from 0 in vacuum to C^0_{ijkl} in the thin film. This sharp transition of $C_{ijkl}(\mathbf{r})$ is smoothened using a function $g(\zeta) = 0.5(1 + \frac{\tanh 2\zeta(\mathbf{r})-1}{2\gamma})$ to avoid mechanical instability, where γ is the deciding parameter for the interfacial thickness between the thin film and the vacuum[4–6]. Thus, $C_{ijkl}(\mathbf{r})$ is expressed as a function of $\zeta(\mathbf{r})$ and it takes the form as $C_{ijkl}(\mathbf{r}) = C^0_{ijkl} g(\zeta)$. The elastic energy for the inhomogeneous system can be written as

$$f_{ela} = \frac{1}{2} \int C_{ijkl}(\mathbf{r})(\epsilon_{ij} - \epsilon^{0G}_{ij})(\epsilon_{kl} - \epsilon^{0G}_{kl}) dV \tag{S1}$$

We employ an iterative phase-field microelasticity solver to determine the stress field for this inhomogeneous system by considering an equivalent system with a homogeneous modulus C^0_{ijkl} and an effective stress-free strain ϵ^{eff}_{ij} defined by[4,5]

$$C^0_{ijkl}\Big(\epsilon_{kl}(\mathbf{r}) - \epsilon^{eff}_{kl}(\mathbf{r})\Big) = C_{ijkl}(\mathbf{r})\Big(\epsilon_{kl}(\mathbf{r}) - \epsilon^{0G}_{kl}(\mathbf{r})\Big) \tag{S2}$$

The equivalent elastic energy considering the effective strain is written as follows:[5,7]

$$\begin{aligned} E^{eq}_{el} &= \frac{1}{2} \int C^0_{ijkl} \epsilon^{eff}_{ij} \epsilon^{eff}_{kl} d^3r + \frac{1}{2} \int C^0_{ijkl} E_{ij} E_{kl} d^3r \\ &- E_{ij} \frac{1}{2} \int C^0_{ijkl} \epsilon^{eff}_{kl} d^3r - \frac{1}{2} \int_{k=0} \frac{d^3r}{(2\pi)^3} \times k_i \tilde{\sigma}^{eff}_{ij(\mathbf{k})} \tilde{G}_{jk}(\mathbf{k}) \tilde{\sigma}^{eff}_{kl}(\mathbf{k}) k_l \\ &+ \frac{1}{2} \int_V (C^0_{ijmn} \Delta S_{mnpq} C^0_{pqkl} - C^0_{ijkl}) \times (\epsilon^{eff}_{ij} - \epsilon^{0G}_{ij})(\epsilon^{eff}_{kl} - \epsilon^{0G}_{kl}) d^3r, \end{aligned} \tag{S3}$$

where V is the system volume, $G_{jk}(\mathbf{k})$ is Green's function tensor, and k_i are the components of the directional vector in the Fourier space. $\Delta S_{mnpq} = [C^0_{mnpq} - C_{mnpq}(\mathbf{r})]^{-1}$ and $\sigma^{eff}_{ij}(\mathbf{k})$ is the effective stress expressed as $\sigma^{eff}_{ij}(\mathbf{k}) = C^0_{ijkl} \int_V \epsilon^{eff}_{kl}(\mathbf{r}) e^{-i\mathbf{k}\cdot\mathbf{r}} d^3r$. The effective strain can be obtained by setting the functional variation of the equivalent elastic energy with respect to the effective strain ($\frac{\delta E^{eq}_{el}}{\delta \epsilon^{eff}_{ij}} = 0$) and solving the TDGL type equation:[4–7]

$$\frac{\partial \epsilon^{eff}_{ij}}{\partial t} = -K_{ijkl} \cdot \frac{\delta E^{eq}_{el}}{\delta \epsilon^{eff}_{kl}} \tag{S4}$$

Here, the kinetic coefficient K_{ijkl} is a tensor proportional to the modulus variation and assumed to be $K_{ijkl} = K S^0_{ijkl}$ for simplicity, where S^0_{ijkl} is the homogeneous elastic compliance tensor and K is a constant. The elastic strains and stresses are obtained from the effective strain as follows:

$$\begin{gathered} \epsilon_{ij}(\mathbf{r}) = E_{ij} + \frac{1}{2} \int_{\mathbf{k}=0} \frac{d^3k}{(2\pi)^3} (k_i \tilde{G_{jk}} + k_j \tilde{G_{ik}}) \tilde{\sigma^{eff}_{kl}}(\mathbf{k})^* k_l e^{-i\mathbf{k}\cdot\mathbf{r}} \\ \sigma_{ij}(\mathbf{r}) = C^0_{ijkl}\Big(\epsilon_{kl}(\mathbf{r}) - \epsilon^{eff}_{kl}(\mathbf{r})\Big) \end{gathered} \tag{S5}$$

S2 Derivation of stresses under plane stress state

The sum of contributions of the elastic energy and electrostrictive energy in a single grain can be expressed as

$$
\begin{aligned}
G = &-\frac{1}{2}S_{11}\sigma_1^2 - \frac{1}{2}S_{22}\sigma_2^2 - \frac{1}{2}S_{33}\sigma_3^2 - S_{12}\sigma_1\sigma_2 - S_{23}\sigma_2\sigma_3 - S_{13}\sigma_3\sigma_1 - \frac{1}{2}S_{44}\sigma_4^2 - \frac{1}{2}S_{55}\sigma_5^2 - \frac{1}{2}S_{66}\sigma_6^2 \\
&- (Q_{13}\sigma_1 + Q_{23}\sigma_2 + Q_{33}\sigma_3)P_{Zi}^2
\end{aligned} \tag{S6}
$$

Elastic equations of state could be obtained by the minimization $\delta G/\delta\sigma_{ij} = -\mu_{jk}$. The equations of state have the form:

$$
\begin{aligned}
\tilde{\mu_1} - \mu_1 &= S_{11}\sigma_1 + S_{12}\sigma_2 + S_{13}\sigma_3 \\
\tilde{\mu_2} - \mu_2 &= S_{12}\sigma_1 + S_{22}\sigma_2 + S_{23}\sigma_3 \\
\tilde{\mu_3} - \mu_3 &= S_{13}\sigma_1 + S_{23}\sigma_2 + S_{33}\sigma_3 \\
\tilde{\mu_4} - \mu_4 &= S_{44}\sigma_4 \\
\tilde{\mu_5} - \mu_5 &= S_{44}\sigma_5 \\
\tilde{\mu_6} - \mu_6 &= S_{44}\sigma_6,
\end{aligned} \tag{S7}
$$

Here, μ_i are the designations of the strains in the absence of stresses obtained from the electrostrictive contributions of the energy:

$$
\begin{aligned}
\mu_1 &= Q_{13}P_{Zi}^2 \\
\mu_2 &= Q_{23}P_{Zi}^2 \\
\mu_3 &= Q_{33}P_{Zi}^2 \\
\mu_4 &= \mu_5 = \mu_6 = 0
\end{aligned} \tag{S8}
$$

Compatibility relation $e_{ikl}e_{jmn}(\delta^2\tilde{\mu}_{ln}/\delta x_k x_n) = 0$ leads to the conditions of constant strains $\tilde{\mu_1}$=const, $\tilde{\mu_2}$=const, and $\tilde{\mu_6}$=cont. Setting constant strains to values of spontaneous polarization in stress free, homogeneous system, we obtain

$$
\begin{aligned}
\tilde{\mu_1} &= \mu_1^S = Q_{13}P_0^2 \\
\tilde{\mu_2} &= \mu_2^S = Q_{23}P_0^2 \\
\tilde{\mu_3} &= \mu_3^S = Q_{33}P_0^2
\end{aligned} \tag{S9}
$$

Considering plane stress state $\sigma_3 = 0$, we modify Eqns. S7 to

$$
\begin{aligned}
S_{11}\sigma_1 + S_{12}\sigma_2 &= \mu_1^S - \mu_1 \\
S_{12}\sigma_1 + S_{22}\sigma_2 &= \mu_2^S - \mu_2 \\
S_{13}\sigma_1 + S_{23}\sigma_2 &= \mu_3^S - \mu_3
\end{aligned} \tag{S10}
$$

Substituting Eqns. S8 and S9 in Eqn. S10, we obtain the unknown stress components:

$$
\begin{aligned}
\sigma_1 &= \frac{(S_{22}Q_{13} - S_{12}Q_{23})(P_0^2 - P_{Zi}^2)}{S_{11}S_{22} - S_{12}^2} \\
\sigma_2 &= \frac{(S_{11}Q_{23} - S_{12}Q_{13})(P_0^2 - P_{Zi}^2)}{S_{11}S_{22} - S_{12}^2}
\end{aligned} \tag{S11}
$$

S3 Calibration of Landau coefficients

The Landau coefficients for HZO are obtained by fitting polarization hysteresis function $P(E)$ with measured PE curve for 10 nm-thick $\mathrm{Hf_{0.5}Zr_{0.5}O_2}$ film. $P(E)$ is the inverse of the following function:

$$E = 2a_1P + 4a_{11}P^3 + 6a_{111}P^5 \tag{S12}$$

We obtain two sets of Landau coefficients considering first order and second order phase transitions, which are distinguished by the sign of coefficient a_{11}: $a_{11} < 0$ for 1^{st} order and $a_{11} > 0$ for 2^{nd} order transitions. The extracted Landau coefficients are given in **Table S1** .

Landau coefficients	Set I ($a_{11} < 0$)	Set II ($a_{11} > 0$)
a_1	$-2.976 \times 10^8\ \frac{Jm}{C^2}$	$-4.835 \times 10^8\ \frac{Jm}{C^2}$
a_{11}	$-2.160 \times 10^8\ \frac{Jm^5}{C^4}$	$4.367 \times 10^9\ \frac{Jm^5}{C^4}$
a_{111}	$1.653 \times 10^{10}\ \frac{Jm^9}{C^6}$	$6.687 \times 10^9\ \frac{Jm^9}{C^6}$

Table S1: Landau coefficients extracted from the measured PE curve for 10 nm-thick $\mathrm{Hf_{0.5}Zr_{0.5}O_2}$ film.

The comparison of polarization hysteresis functions for two sets (Set 1: $a_{11} < 0$ and Set 2: $a_{11} > 0$) of Landau coefficients with the measured PE curve is shown in **Figure S1**. Since ferroelectric HZO is well described by first order phase transition formalism, we consider the first set ($a_{11} < 0$) of Landau coefficients for the phase field simulations.

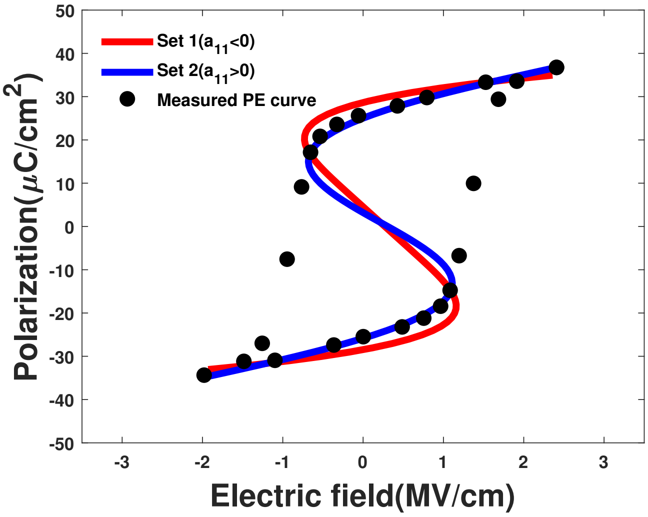

Figure S1: Comparison of calibrated polarization hysteresis functions for $a_{11} < 0$ (Set 1) and $a_{11} > 0$ (Set 2) with the measured PE curve. Measured PE curve reprinted (adapted) with permission from (Kim, Si Joon, et al. *ACS applied materials & interfaces* 11.5 (2019): 5208-5214)[8]. Copyright (2019) American Chemical Society.

S4 Optimization of Landau coefficients by genetic algorithm

Two sets of optimized Landau coefficients are obtained using the genetic algorithm by considering first order and second order transitions. The optimized Landau coefficients are listed in **Table S2**.

The comparison of polarization hysteresis functions and simulated PE curves for two sets (Set 1: $a_{11} < 0$ and Set2: $a_{11} > 0$) of GA optimized Landau coefficients are presented in **Figure S2a** and **Figure S2b**, respectively. The calculated values of the

Landau coefficients	Set I ($a_{11} < 0$)	Set II ($a_{11} > 0$)
a_1	$-4.289 \times 10^8 \ \frac{Jm}{C^2}$	$-4.754 \times 10^8 \ \frac{Jm}{C^2}$
a_{11}	$-2.242 \times 10^8 \ \frac{Jm^5}{C^4}$	$2.848 \times 10^7 \ \frac{Jm^5}{C^4}$
a_{111}	$2.170 \times 10^9 \ \frac{Jm^9}{C^6}$	$1.776 \times 10^9 \ \frac{Jm^9}{C^6}$

Table S2: Landau coefficients optimized by genetic algorithm.

objective functions are 0.00109 for Set 1 and 0.00103 for Set 2. The values of objective function of the highest ranked chromosome in each generation for both sets of GA simulations are shown in **Figure S3**. Here, we consider the first set ($a_{11} < 0$) of Landau coefficients describing first order phase transition for the phase field simulations.

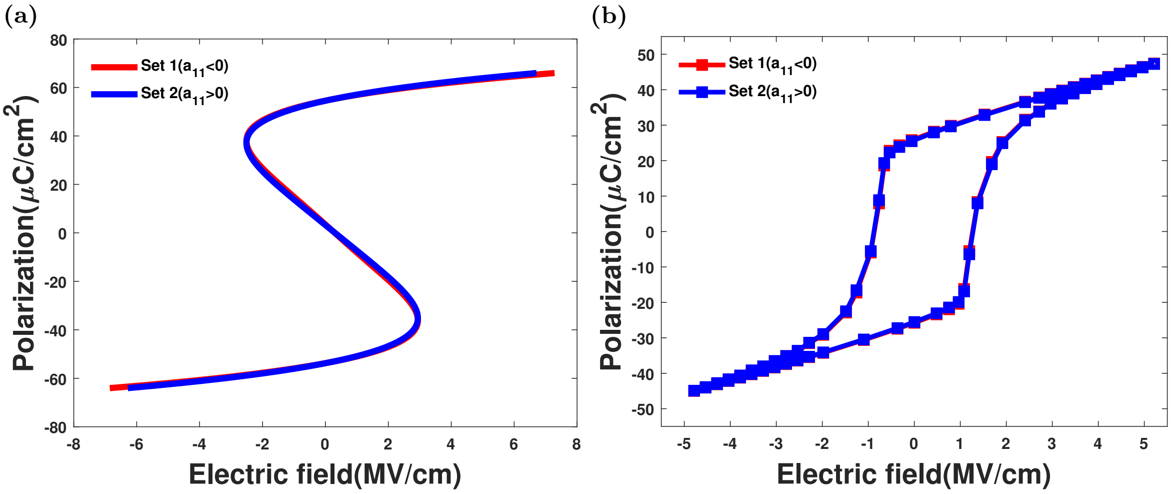

Figure S2: (a) Comparison of GA optimized polarization hysteresis functions for $a_{11} < 0$ (Set 1) and $a_{11} > 0$ (Set 2). (b) Comparison of simulated PE curves using the same two sets of GA optimized Landau coefficients.

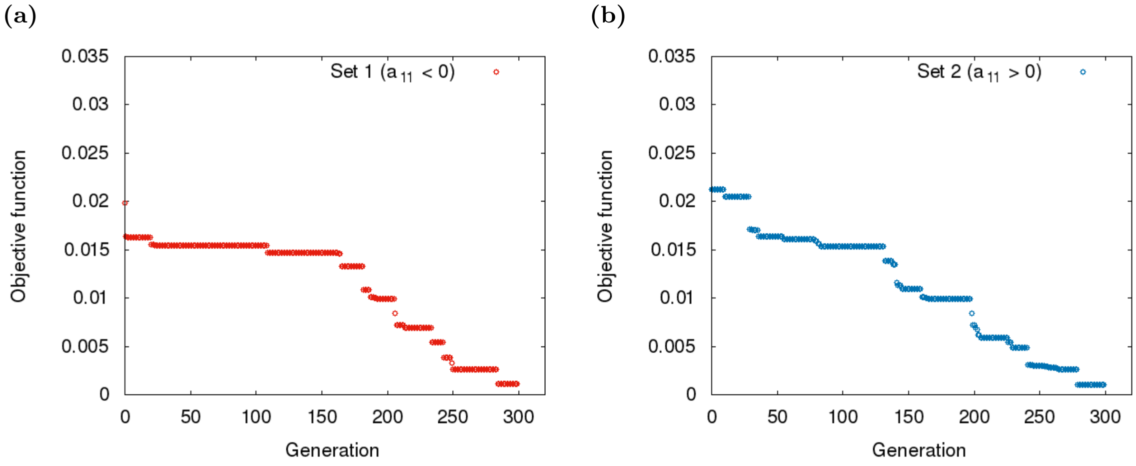

Figure S3: The values of objective function for the highest ranked chromosome in each generation plotted across all the generations for (a) $a_{11} < 0$ (Set 1) and (b) $a_{11} > 0$ (Set 2)

S5 Estimation of spontaneous polarization and dielectric permittivity of HZO from GA optimized effective Landau coefficients

The single-domain ground state property of the HZO including the spontaneous polarization and dielectric permittivity are calculated from the GA optimized Landau coefficients. The spontaneous polarization P_0 is obtained from Landau coefficients using the following expression: [9]

$$P_0 = \pm\sqrt{-\frac{a_{11}\left(1+\sqrt{1-\frac{3a_1a_{111}}{a_{11}^2}}\right)}{3a_{111}}} \tag{S13}$$

The dielectric permittivity ϵ_r is calculated from the expression [10]

$$\epsilon_r = \frac{1}{3\sqrt{3}}\frac{P_0}{\epsilon_0 E_c}, \tag{S14}$$

where E_c is the coercive field estimated from the given expression: [9]

$$E_c = \frac{8}{25}\sqrt{\frac{|a_{11}|^5}{5a_{111}^3}}\sqrt{1+\sqrt{1-\frac{5a_1a_{111}}{a_{11}^2}}}\left(1-\frac{5a_1a_{111}}{a_{11}^2}+\sqrt{1-\frac{5a_1a_{111}}{a_{11}^2}}\right) \tag{S15}$$

S6 Normalization of applied electric fields

For better comparison of the domain dynamics during switching in phase field simulations and experimental observations, the applied electric fields are normalized with respect to corresponding switching voltages. The switching regions are estimated from the fraction of up and down polar domains in the domain structures at different applied fields. The reversal of polarization from up to down domains occurs from $-1.2\ \frac{MV}{cm}$ to $-1.8\ \frac{MV}{cm}$ in experiments and from $-0.75\ \frac{MV}{cm}$ to $-2.25\ \frac{MV}{cm}$ in simulations. Similarly, polarization reversal from down to up domains occurs from $1.2\ \frac{MV}{cm}$ to $1.8\ \frac{MV}{cm}$ in experiments and from $0.75\ \frac{MV}{cm}$ to $2.25\ \frac{MV}{cm}$ in simulations. The normalized applied field E^* is calculated using the following expressions:

$$E^* = \frac{5}{3}\left(1-\frac{3}{5|E_{exp}|}\right)E_{exp}, \tag{S16}$$

$$E^* = \frac{4}{7}\left(1+\frac{1}{|E_{pfm}|}\right)E_{pfm}, \tag{S17}$$

where, E_{exp} and E_{pfm} are the applied electric fields in experiments and simulations, respectively. The electric fields applied on the thin film in simulations and experiments corresponding to the values of normalized applied fields for domain structures illustrated in **Figure 4** are listed in **Table S3**.

E^*	$E_{exp}(MV/cm)$	$E_{pfm}(MV/cm)$
-1.2	-1.3	-1.0
-1.3	-1.4	-1.3
-1.5	-1.5	-1.6
-1.8	-1.7	-2.2
1.2	1.3	1.0
1.3	1.4	1.3
1.5	1.5	1.6
1.8	1.7	2.2

Table S3: Applied electric fields in simulations and experiments corresponding to values of normalized applied fields for domain structures in Figure 4

S7 Simulation of polarization profiles across a 180° domain wall and switching curves in a bulk single crystal using calibrated effective Landau coefficients and corresponding Landau coefficients

The calibrated effective Landau coefficients ($a_1 = -2.976 \times 10^8\ \frac{Jm}{C^2}$, $a_{11} = -2.160 \times 10^8\ \frac{Jm^5}{C^4}$, and $a_{111} = 1.653 \times 10^{10}\ \frac{Jm^9}{C^6}$) are used to simulate polarization profiles across a 180° domain wall and polarization switching in a bulk single crystal (two-dimensional). Further, we perform the simulations using Landau coefficients considering elastic energy and compare both results. The Landau coefficients estimated from the calibrated effective coefficients are: $\alpha_1 = -2.749 \times 10^8\ \frac{Jm}{C^2}$, $\alpha_{11} = -4.933 \times 10^8\ \frac{Jm^5}{C^4}$, and $\alpha_{111} = 1.653 \times 10^{10}\ \frac{Jm^9}{C^6}$. The polarization profiles for the two domain system for both sets of coefficients are compared in **Figure S4**. The values of steady-state polarizations in 180° domains are matching for the effective Landau coefficients and corresponding Landau coefficients. The comparison of switching curves in bulk single crystal for both sets of coefficients are given in **Figure S5**. The PE curves are also similar for the effective Landau coefficients and corresponding Landau coefficients except for some discrepancies in the coercive field. This shows good agreement of the strain-polarization coupling with the free energy coefficients.

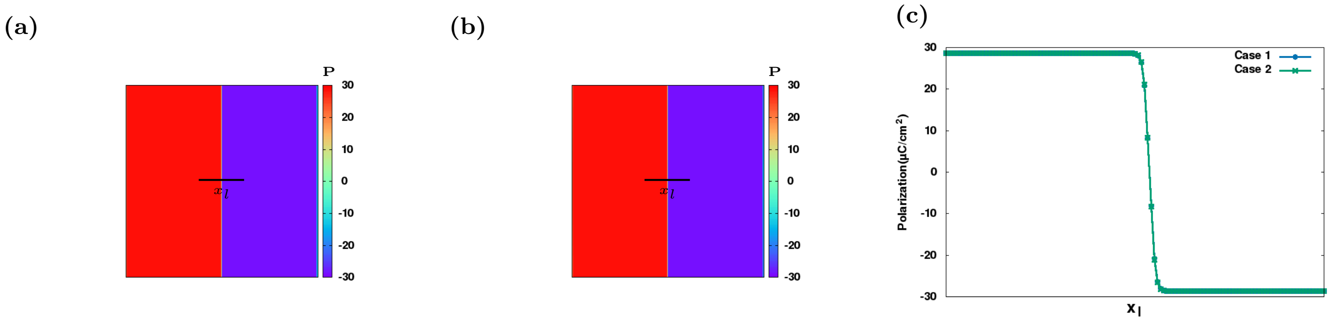

Figure S4: Polarization profiles across a 180° domain wall simulated using (a) calibrated effective Landau coefficients (Case 1) and (b) corresponding Landau coefficients (Case 2). (c) Comparison of the polarization profiles (1D) for Case 1 and Case 2 along a line x_l drawn across the domain walls.

S8 Estimation of susceptibility of the non-ferroelectric phase (χ_d)

To study the impact of the ferroelectric phase fraction of HZO thin films on switching characteristics, the susceptibility of the non-ferroelectric phase is obtained from the measured PE curve of 10 nm-thick HfO$_2$ film. PE curves are generated using a phase field model for non-ferroelectric columnar thin films with bulk free energy expressed as follows:

$$f_{bulk} = \sum_{i=1}^{N} h(\phi_i) f_{Di}, \tag{S18}$$

where N is the total number of grains. We estimate the value of dielectric susceptibility at which the simulated PE curve matches the experimentally calculated PE curve for non-ferroelectric hafnia thin film. The fit between simulated and measured PE curves are demonstrated in **Figure S6** and the estimated value of χ_d is $2.108 \times 10^{-10}\ \frac{C^2}{Jm}$.

S9 Comparison of PE curves of [001] textured film and single crystalline HZO.

We compare the PE curve for [001] textured film with the PE curve for single crystalline HZO. From **Figure S7**, it is evident that there are discrepancies between the switching characteristics of [001] textured thin film and single crystalline HZO. Even though the

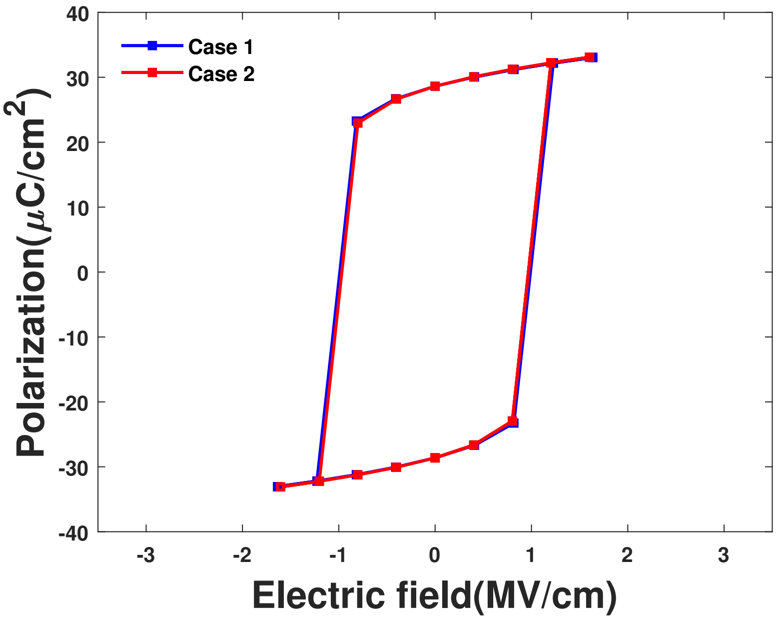

Figure S5: Comparison of PE curves for single crystal simulated using calibrated effective Landau coefficients in the absence of elastic interactions (Case 1) and corresponding Landau coefficients considering elastic interactions (Case 2).

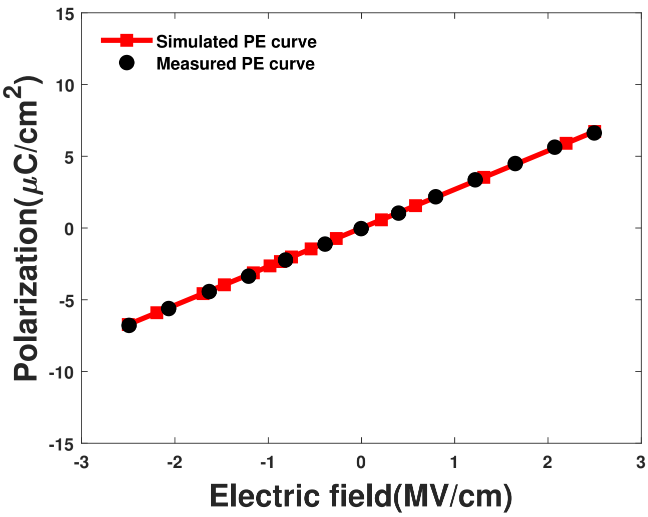

Figure S6: Comparison of simulated PE curve for non-ferroelectric columnar thin film and experimentally measured curve for 10 *nm*-thick HfO_2 film. Measured PE curve reprinted (adapted) with permission from (Kim, Si Joon, et al. *ACS applied materials & interfaces* 11.5 (2019): 5208-5214)[8]. Copyright (2019) American Chemical Society.

remnant polarizations for both curves are similar, the coercive field and polarization switching slopes are different. This mismatch in coercive field and polarization switching slope can be due to the reduced degree of preferred orientation in the textured thin film. When the orientations of grains in the textured film deviates from the preferred orientation, the non-polar contributions of the free energy $\left(1/2\chi_f(P_{Xi}^2 + P_{Yi}^2)\right)$ affects the polarization switching modifying coercive field and switching slope. Because of its quadratic form, the non-ferroelectric contribution cannot significantly influence the switching curve in the absence of any external field. Therefore, the remnant polarizations for both [001] textured thin film and single crystalline HZO remain similar.

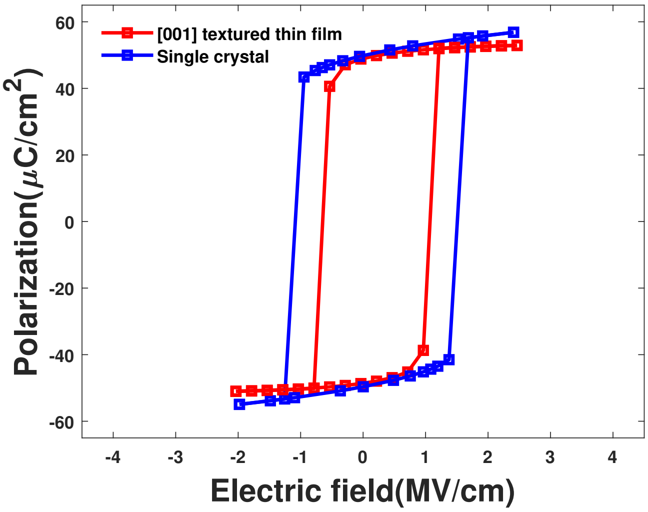

Figure S7: Comparison of simulated PE curve for [001] textured thin films with the PE curve of single crystalline HZO.

S10 Effect of grain size on switching characteristics

Simulations are performed on 10 nm-thick columnar films of different grain sizes ($D = 60, 90$ and 120 nm) to investigate the impact of grain size on switching dynamics. **Table S4** provides the simulation parameters used for the study. The grain size dependent behaviour of PE curves are illustrated in **Figure S8**. It shows that the switching characteristics do not significantly change with the variation in grain sizes. With an increase in grain size, remnant polarization increases, but the coercive field remains almost the same (~ 1.1 $\frac{MV}{cm}$). Thin films with grain sizes of $60, 90$ and 120 nm exhibit P_r values of ~ 25.86 $\frac{\mu C}{cm^2}$, ~ 28.21 $\frac{\mu C}{cm^2}$, and ~ 29.66 $\frac{\mu C}{cm^2}$, respectively.

The reduced remnant polarization in thin films with finer grains can be attributed to the increase in the proportion of grain boundaries with the decrease in grain size. The grain boundaries may distort ferroelectric switching because of their paraelectric nature. But, the prediction of enhancement in ferroelectricity in thin films with coarser grains from our simulations seemed to contradict other theoretical and experimental observations[11,12]. The thin films with coarser grains show reduced ferroelectricity because of crossover of HZO from ferroelectric orthorhombic phase to non-ferroelectric monoclinic phase for an average grain size above 16 nm[11]. But, we have not considered the change of ferroelectric orthorhombic phase to non-ferroelectric monoclinic phase with an increase in grain size in our model as reported in experiments[13,14]. The grains in the simulated polycrystalline structure are assumed to be 100% ferroelectric. Therefore, it is difficult to draw clear conclusions on the effect of grain size on switching characteristics from our model.

To investigate the effect of grain size on switching dynamics, we use 20 nm-thick films with an equiaxed grain morphology and different grain sizes ($D = 20, 30$ and 40 nm). GA optimized Landau coefficients are used in the simulations and the parameters are listed in **Table S5**. The comparison of simulated PE curves for thin films with different grain sizes is illustrated in **Figure S9**.

Following the trend seen in columnar thin films, remnant polarization increases from ~ 22.80 $\frac{\mu C}{cm^2}$ to ~ 25.65 $\frac{\mu C}{cm^2}$ and the coercive field remains essentially the same at ~ 1.3 $\frac{MV}{cm}$, when the grain size is varied from 20 to 30 nm. A further increase in

Parameters	
Thin film surface area ($\Delta X \times \Delta Y$)	$1280 \times 1280, 2240 \times 2240, 2688 \times 2688\ nm^2$
Thin film thickness (t_Z)	$10\ nm$
Effective Landau coefficient (a_1)	$-4.289\ \times 10^8 \frac{Jm}{C^2}$
Effective Landau coefficient (a_{11})	$-2.242 \times 10^8\ \frac{Jm^5}{C^4}$
Effective Landau coefficient (a_{111})	$2.170 \times 10^9\ \frac{Jm^9}{C^6}$
Background dielectric susceptibility (χ_f)	$4.019 \times 10^{-10}\ \frac{C^2}{Jm}$
Gradient energy coefficient (G_{11})	$5.066 \times 10^{-10}\ \frac{Jm^3}{C^2}$
Average grain size (D)	$60, 90, 120\ nm$
Number of grains (N)	$480, 492, 496$

Table S4: Simulation parameters used to investigate the effect of grain size in thin films with columnar grain morphology.

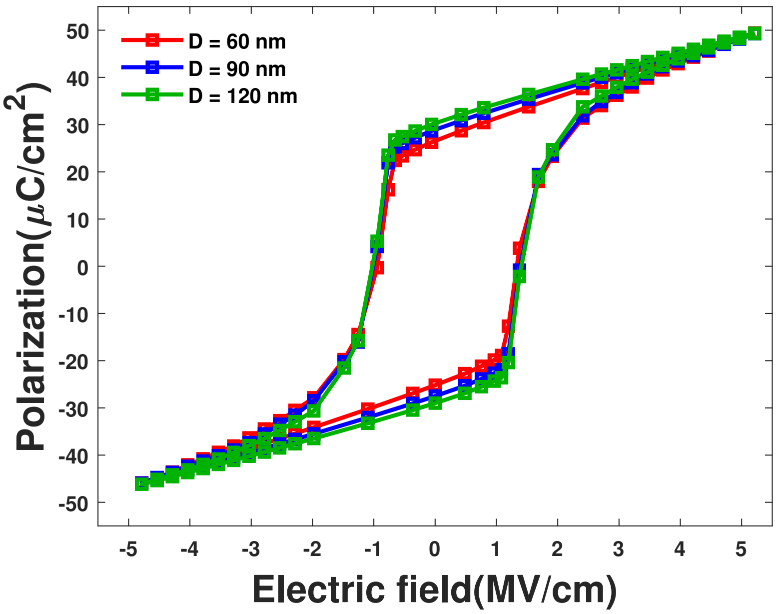

Figure S8: Effect of grain size on switching characteristics. Comparison of simulated PE curves for columnar thin films ($t_F = 10\ nm$) with different grain sizes ($D = 60, 90, 120\ nm$).

Parameters	
Thin film surface area ($\Delta X \times \Delta Y$)	$480 \times 480, 800 \times 800, 1200 \times 1200\ nm^2$
Thin film thickness (t_Z)	$20\ nm$
Effective Landau coefficient (a_1)	$-4.289 \times 10^8\ \frac{Jm}{C^2}$
Effective Landau coefficient (a_{11})	$-2.242 \times 10^8\ \frac{Jm^5}{C^4}$
Effective Landau coefficient (a_{111})	$2.170 \times 10^9\ \frac{Jm^9}{C^6}$
Background dielectric susceptibility (χ_f)	$4.019 \times 10^{-10}\ \frac{C^2}{Jm}$
Gradient energy coefficient (G_{11})	$5.066 \times 10^{-10}\ \frac{Jm^3}{C^2}$
Average grain size (D)	$20, 30, 40\ nm$
Number of grains (N)	$427, 620, 756$

Table S5: Simulation parameters to study the effect of grain size in thin films with equiaxed grain morphology.

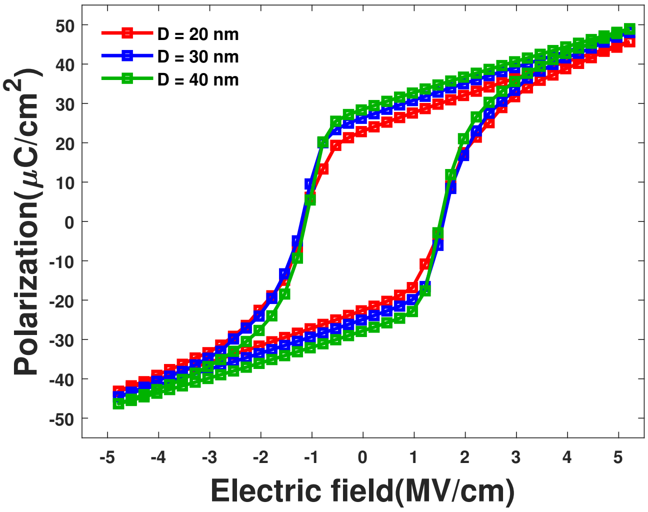

Figure S9: Effect of grain size on switching characteristics. Comparison of simulated PE curves for 20 nm-thick equiaxed films with different grain sizes ($D = 20, 30, 40$ nm).

grain size to 40 nm also increases the remnant polarization to $\sim 28.16\ \frac{\mu C}{cm^2}$, but the coercive field decreases to $\sim 1.2\ \frac{MV}{cm}$. This variation in switching characteristics can be explained by the change in grain morphology from an equiaxed to a columnar structure with an increase in grain size. When the average grain size increases beyond thin film thickness, the equiaxed grain structure tends to become columnar. This is evident from the side views (ZX plane) of the simulated microstructure of the thin films shown in **Figure S10**.

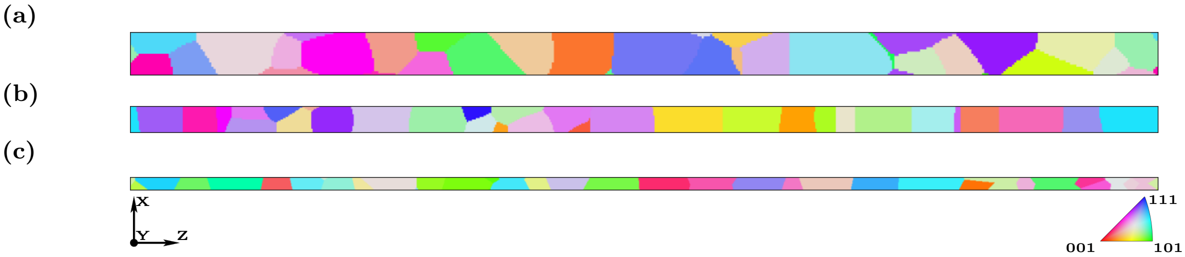

Figure S10: Side views (ZX plane) of the simulated microstructure of 20 nm-thick equiaxed films with different grain sizes: (a) 20, (b) 30, and (c) 40 nm.

The increase in remnant polarization with the increase in grain size from 20 to 30 nm is due to the decreasing proportion of grain boundaries when the grain size increases. Whereas, the increase in remnant polarization and decrease in the coercive field with a further increase in grain size to 40 nm can be attributed to the change in grain morphology of the thin film.

References

[1] Wheeler, A. A., Boettinger, W. J. & McFadden, G. B. Phase-field model for isothermal phase transitions in binary alloys. *Physical Review A* **45**, 7424 (1992).

[2] Kobayashi, R. Modeling and numerical simulations of dendritic crystal growth. *Physica D: Nonlinear Phenomena* **63**, 410–423 (1993).

[3] Karma, A. Phase-field model of eutectic growth. *Physical Review E* **49**, 2245 (1994).

[4] Wang, Y. U., Jin, Y. M. & Khachaturyan, A. G. Phase field microelasticity theory and modeling of elastically and structurally inhomogeneous solid. *J. Appl. Phys.* **92**, 1351–1360 (2002).

[5] Wang, Y. U., Jin, Y. M. & Khachaturyan, A. G. Phase field microelasticity modeling of surface instability of heteroepitaxial thin films. *Acta Mater.* **52**, 81–92 (2004).

[6] Saj Mohan, M., Bandyopadhyay, S., Jogi, T., Bhattacharya, S. & Ramadurai, R. Realization of rhombohedral, mixed, and tetragonal like phases of $BiFeO_3$ and ferroelectric domain engineering using a strain tuning layer on $LaAlO_3$ (001) substrate. *J. Appl. Phys.* **125**, 012501 (2019).

[7] Ni, Y., He, L. & Soh, A. Three-dimensional phase field simulation for surface roughening of heteroepitaxial films with elastic anisotropy. *J. Cryst. Growth* **284**, 281–292 (2005).

[8] Kim, S. J. *et al.* Stress-induced crystallization of thin $Hf_{(1-X)}Zr_XO_2$ films: The origin of enhanced energy density with minimized energy loss for lead-free electrostatic energy storage applications. *ACS Appl. Mater. Interfaces* **11**, 5208–5214 (2019).

[9] Ducharme, S. *et al.* Intrinsic ferroelectric coercive field. *Phys. Rev. Lett.* **84**, 175 (2000).

[10] Kashir, A., Farahani, M. G., Lancok, J., Hwang, H. & Kamba, S. A grease for domain walls motion in HfO_2-based ferroelectrics. *Nanotechnology* (2021).

[11] Materlik, R., Künneth, C. & Kersch, A. The origin of ferroelectricity in hf1- xzrxo2: A computational investigation and a surface energy model. *Journal of Applied Physics* **117**, 134109 (2015).

[12] Mimura, T., Shimizu, T., Sakata, O. & Funakubo, H. Thickness dependence of phase stability in epitaxial (hf x zr 1- x) o 2 films. *Physical Review Materials* **5**, 114407 (2021).

[13] Kim, H. J. *et al.* Grain size engineering for ferroelectric $Hf_{0.5}Zr_{0.5}O_2$ films by an insertion of Al_2O_3 interlayer. *Appl. Phys. Lett.* **105**, 192903 (2014).

[14] Shandalov, M. & McIntyre, P. C. Size-dependent polymorphism in HfO_2 nanotubes and nanoscale thin films. *J. Appl. Phys.* **106**, 084322 (2009).